Check for updates

Enhanced electrochemical sensing of lead in environmental samples using Bi₂O₃/IL/rGO hybrid nanocomposite

Sanoober Bhagat,[a] Sana-ul-Nisa,[ab] Tania Ghumro,[b] Jamil A. Buledi,[a] Amber R. Solangi ⓘ *[a] and S. Tufail H. Sherazi[a]

The current study uses the ionic liquid (IL) 1-butyl-3-methylimidazolium hexafluorophosphate, also known as BMIM-PF₆, as a stabilizing agent to synthesize a bismuth oxide/ionic liquid/reduced graphene oxide (Bi₂O₃/IL/rGO) hybrid nanomaterial. A range of techniques, including scanning electron microscopy (SEM), X-ray diffraction (XRD), energy dispersive X-ray spectroscopy (EDX), Fourier transform infrared spectroscopy (FTIR), and UV-visible spectroscopy, were used to characterize the synthesized Bi₂O₃/IL/rGO nanocomposite. XRD confirmed that the composite was crystalline, and FTIR analysis suggested the presence of certain functional groups. The main elements oxygen, carbon, and bismuth were confirmed by EDX analysis, and SEM imaging showed an exfoliated and detached morphology. The synthesized nanocomposite was used to modify a glassy carbon electrode to develop a sensor for the detection of lead (Pb^{2+}). The fabricated sensor was characterized using electrochemical impendence spectroscopy (EIS) and cyclic voltammetry (CV). The results indicated that the Bi₂O₃/IL/rGO/GCE was more conductive, having a charge transfer resistance (R_{ct}) of 428.5 Ω compared to 1870 Ω for the bare electrode. The sensor has a low detection limit of 0.001 μM and a quantification limit of 0.003 μM. When tested on water and soil samples, the sensor was confirmed to have acceptable recovery rates, ranging from 95% to 102%. In conclusion, our fabricated sensor has excellent performance in terms of ease, affordability, energy usage, and quick efficiency.

1. Introduction

Environmental pollution produced by various human activities continues to pose a lethal threat to human health, ecosystems, and biodiversity.[1] Heavy metals are highly concerning pollutants that are released into the environment through industrial processes such as mining, manufacturing, and waste disposal.[2] These metals, especially lead (Pb^{2+}), have become major impurities due to their presence in the environment and their destructive effects on human health.[3] Chronic exposure to lead can result in severe damage to vital organs, including the kidneys and nervous system, making its detection in environmental samples crucial for ensuring public safety.[4] Traditional methods for detecting trace amounts of Pb^{2+} in environmental samples include atomic absorption spectrometry (AAS), inductively coupled plasma optical emission spectrometry (ICP-OES), and inductively coupled plasma mass spectrometry (ICP-MS).[5] While these methods are highly precise, they often require costly equipment and extensive sample preparation. In recent

years, electrochemical sensors have gained consideration due to their cost-effectiveness, portability, and high sensitivity. Among the various electrochemical techniques, voltammetric methods, including differential pulse voltammetry (DPV), have been established as promising approaches for the detection of Pb^{2+} ions.[6] Recent developments in nanomaterials have significantly enhanced the electrochemical performance of sensors, increasing their sensitivity and selectivity for detecting heavy metals like Pb^{2+}.[7] One such material is bismuth oxide (Bi_2O_3), which has demonstrated great potential in heavy metal sensing applications due to its favorable electrochemical properties.[8] The environmentally friendly electrode material bismuth oxide offers great reproducibility, a wide linear detection range, and a promising signal-to-background ratio.[9] Nevertheless, its limited surface area and poor electronic conductivity can hinder its performance in electrochemical sensors.[10] To overcome these limitations, researchers have turned to hybrid nanomaterials combining bismuth oxide with new materials that improve its electrochemical properties.[11] One favorable approach is the combination of bismuth oxide with reduced graphene oxide (rGO) and ionic liquids (ILs).[12] Graphene-based materials, such as rGO, are known for their great surface area, outstanding electrical conductivity, and high mechanical strength.[13] When integrated with bismuth oxide, these

[a]*National Centre of Excellence in Analytical Chemistry, University of Sindh, Jamshoro 76080, Pakistan. E-mail: amber.solangi@usindh.edu.pk*

[b]*Department of Human and Rehabilitation Science, Begum Nusrat Bhutto Women University, Sukkur, Pakistan*

materials dramatically increase the overall electrochemical performance, helping to achieve more efficient electron transfer and enhancing the sensitivity of the sensor.[14] Moreover, ionic liquids, which possess high ionic conductivity and stable electrochemical properties, are useful as effective electrolytes or electrode modifiers, promoting improvement in the performance of the sensor.[15] In this study, we present a novel electrochemical sensor based on a bismuth oxide/ionic liquid/reduced graphene oxide (Bi_2O_3/IL/rGO) hybrid nanomaterial for the sensitive detection of lead ions in environmental samples. The sensor was designed using differential pulse voltammetry (DPV) as the detection method, which enabled the identification of lead ions at low concentrations with high precision. The combination of the Bi_2O_3/IL/rGO hybrid nanomaterial significantly improves the electrochemical response of the sensor compared to a bare electrode, indicating the synergistic effect of the materials in increasing the sensor performance. The modified electrode exhibited high sensitivity, a wide linear detection range, and excellent stability and reproducibility, making it a good candidate for environmental monitoring. To the best of our knowledge, this study is the first to employ a Bi_2O_3/IL/rGO-modified electrode for the electrochemical detection of Pb^{2+} ions and to demonstrate its potential use in real-world applications, such as monitoring lead contamination in wastewater and soil samples. Despite these promising results, there are still certain limitations. The long-term stability of the Bi_2O_3/IL/rGO hybrid sensor can be affected by environmental factors, leading to potential degradation over time. Furthermore, variations in the synthesis of the nanocomposite and variations in environmental conditions may affect the reproducibility of the results. Similarly, while the Bi_2O_3/IL/rGO hybrid significantly improves the performance of the sensor, challenges such as the surface area limits of Bi_2O_3 and potential interference from other substances in real-world samples must still be addressed. However, the Bi_2O_3/IL/rGO hybrid nanocomposite shows considerable potential for large-scale environmental monitoring, offering an efficient and cost-effective alternative to older methods for sensing lead contamination. The combination of Bi_2O_3, IL, and rGO enhances the performance of the sensor through effective electronic conductivity, stability, and sensitivity. Bi_2O_3 enables effective electron transfer, IL helps to stabilize the sensor and also promotes ion exchange, and rGO provides a high surface area for better adsorption and faster electron transfer. The Bi_2O_3/IL/rGO hybrid nanocomposite demonstrates a synergistic combination of bismuth oxide, ionic liquid (IL), and reduced graphene oxide (rGO) for enhanced electrochemical detection. Moreover, the current method provides better sensitivity, selectivity and a lower possible detection limit than the previously reported sensors used for the detection of lead. Together, these materials synergistically increase the ability of the sensor to detect low concentrations of lead with great precision.

2. Materials and methods

In this study, all chemicals used were of analytical grade. Sulfuric acid (H_2SO_4) (MERCK, 7664-93-9, Germany), phosphoric acid (H_3PO_4) (MERCK, 7664-38-2, Germany), graphite, potassium permanganate ($KMnO_4$) (ISOLAB, 7722-64-7, Germany), hydrogen peroxide (H_2O_2) (30 wt%) (MERCK, 1085972500), hydrochloric acid (HCl) (38 wt%) (ISOLAB, 7647-01-0, Germany), and potassium hydroxide (KOH) were sourced from Sigma-Aldrich (USA). Bismuth nitrate pentahydrate ($Bi(NO_3)_3 \cdot 5H_2O$ 99.5%), lead nitrate and sodium hydroxide (NaOH 96.0%) were purchased from Merck (Germany). 1-Butyl-3-methylimidazolium hexafluorophosphate (BMIM-PF$_6$) was obtained from Shanghai Aladdin Co. and used as received without further treatment. A 0.01 M stock solution of lead was prepared using deionized water and stored in a refrigerator. Several buffer solutions were prepared, including Britton–Robinson buffer (BRB), which was prepared by combining 0.1 M acetic acid (100%), 0.1 M phosphoric acid (99–100%), and 0.1 M boric acid (99–100%) as a supporting electrolyte. The pH of the buffer was adjusted to the desired value using 0.1 M NaOH or 0.1 M HCl. A Nafion® solution was obtained from Sigma-Aldrich (Sweden and the UK) and diluted to 0.1% in deionized (DI) water for further use. For the preparation of the lead standard solution, a flask containing 10 mg of lead in 10 mL of solution was used, resulting in a concentration of 1 mg of lead per milliliter. The contents of the flask were thoroughly mixed to prepare a 0.01 M stock solution of lead.

2.1 Synthesis of graphene oxide

Graphene oxide (GO) was synthesized using Hummer's method (Fig. 1). In the reaction step, 35 mL of conc. sulphuric acid (H_2SO_4) and 20 mL of phosphoric acid (H_3PO_4) were mixed at 200 rpm using a magnetic stirrer. During this process, 2 g of graphite and 6 g of potassium permanganate ($KMnO_4$) were gradually added to the prepared solution. The mixture was maintained at a constant temperature of 30–35 °C and stirred for 16 h. After the reaction time, the solution was transferred to a beaker containing 400 g of ice, where it was mixed as part of the quenching step. During the mixing with ice, 3 mL of 30 wt% hydrogen peroxide (H_2O_2) was added drop-by-drop. The presence of white graphite indicated that the reaction had proceeded successfully. If the graphite remained gray or black, the reaction process was restarted. During the washing step, the mixture was centrifuged at 3000 rpm for 45 min, and the acid supernatant was discarded. The resulting pellets were washed sequentially with distilled water, followed by three washes with 38 wt% hydrochloric acid (HCl) and three washes with anhydrous ethanol, all by centrifugation at 5000 rpm for 45 min. Finally, the pellets were dried in an oven. A graphical representation of synthesis of GO is presented in Fig. 1.

2.2 Synthesis of the Bi_2O_3/IL/rGO nanocomposite

100 mg of graphene oxide (GO) was dispersed in 100 mL of deionized water and subjected to ultrasonication for 30 min at room temperature. In a separate container, 1 g of pure Bi_2O_3 was dissolved in 100 mL of deionized water and stirred for 30 min. The prepared pure Bi_2O_3 solution was then added to the GO suspension, which was further sonicated for an additional hour. Subsequently, a 0.5 M KOH solution was introduced into the mixture and
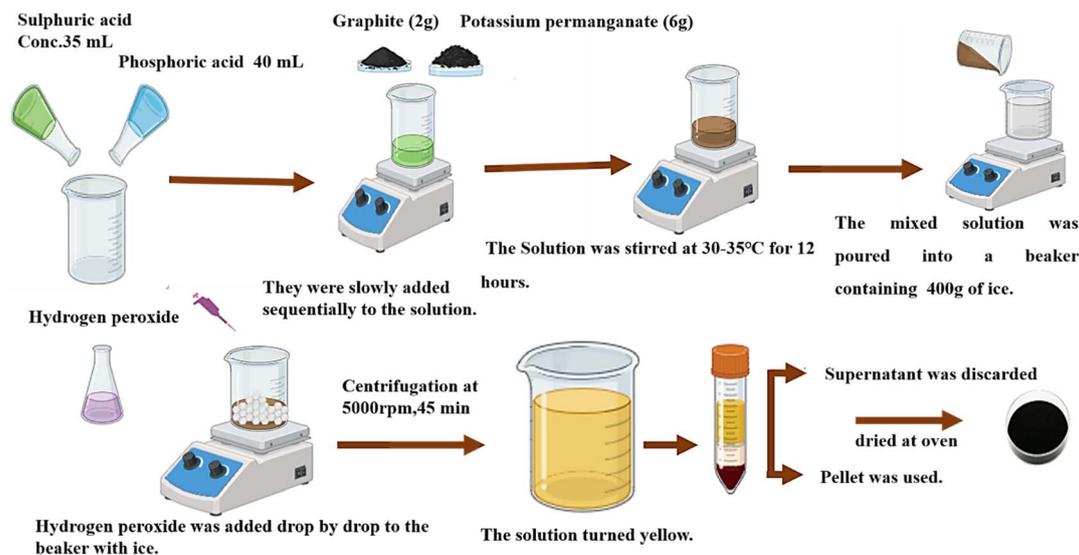
Fig. 1 Graphical representation of the graphene oxide (GO) synthesis using Hummer's method.

monitored under dynamic stirring for 30 min. Afterward, 150 μL of ionic liquid (1-butyl-3-methylimidazolium hexafluorophosphate) (BMIM-PF$_6$) was added as a reducing and coating agent, and the solution was stirred for 2 to 3 h. The resulting ionic liquid/reduced graphene oxide (Bi$_2$O$_3$/IL-rGO) hybrid metal nanocomposite was then washed several times with deionized water using centrifugation. Finally, the product was dried in a vacuum oven at 200 °C for 2 h to obtain the nanoscale material.

2.3 Instrumentation

Various analytical tools were used to confirm the successful fabrication of the Bi$_2$O$_3$/IL/rGO nanohybrid. The UV-vis spectrum was recorded at room temperature using a Shimadzu UV-vis spectrophotometer (Model 365). A thermo Nicolet 5700 Fourier transform infrared spectroscopy (FTIR) instrument was used to analyze the functionality of the material. The crystalline nature of the Bi$_2$O$_3$/IL/rGO nanohybrid was determined through an X-ray diffraction (XRD) using a PANalytical X'Pert PRO, (Almelo, Netherlands). Morphology analysis was conducted *via* scanning electron microscopy (SEM,JEOL,JSM-6380, Japan) associated with energy dispersive X-ray analysis (EDX). Electrochemical measurements were conducted using an advanced electrochemical workstation (CHI 760E), which was interfaced with a personal computer system from CHI Instruments, Inc. (USA). A glassy carbon working (GCE) electrode, a platinum wire counter electrode, and an Ag/AgCl reference electrode made up the traditional three-electrode electrochemical setup.

2.4 Fabrication of the electrochemical sensor

Prior to modification, the surface of a GCE was cleaned with alumina powder and sonicated in ethanol for 20 min to remove some potential impurities. The modification of the bare electrode was conducted with the Bi$_2$O$_3$/IL/rGO material *via* a drop-casting method.[16] In a typical preparation, a suspension of Bi$_2$O$_3$/IL/rGO was prepared by dissolving 3 mg of the material in 3 mL of deionized water, along with 0.1% Nafion® solution as

a binder. This mixture was sonicated for 30 min to provide a constant dispersion. The modified electrode was given the name Bi$_2$O$_3$/IL/rGO/GCE.

2.5 Experimental system for Pb^{2+} detection

In order to detect Pb^{2+} electrochemically, cyclic voltammetry was used at first. The experiments were conducted to examine the redox processes linked to Pb^{2+} within the potential range of −1.0 to 0.0 V. The supporting electrolyte in this experiment was the pH 7 phosphate buffer. The pH of the electrolyte was maintained through the use of NaOH and HCl. For a balanced and accurate calculation of the electrochemical behaviour of Pb^{2+} under specific conditions, a scan rate of 90 mV s^{-1} was chosen.

3. Results and discussion

3.1 UV-visible spectroscopy

The visual properties of graphene oxide (GO) and Bi$_2$O$_3$/IL/rGO were examined using UV-visible spectroscopy.[17] The absorbance spectra were examined in specific wavelength ranges to measure the interactions and electronic transitions of the materials. For graphene oxide, characteristic peaks were observed at 230 nm, demonstrating its unique structural features and electronic properties.[18] The occurrence of the specific absorbance bands suggests the successful synthesis and dispersion of GO. In the case of the bismuth oxide/ionic liquid/reduced graphene oxide, the UV-visible spectrum (265 nm) shown in Fig. 2 reveals distinct absorption characteristics that reproduce its chemical composition and potential applications.[19]

3.2 FTIR analysis of GO and Bi$_2$O$_3$/IL/rGO

FTIR is an effective technique for identifying chemical bonds in complex composite materials. The characteristic absorption peaks of GO in Fig. 3(a), such as those at 3400 cm^{-1} (O–H stretching vibration), 1726 cm^{-1} (C=O stretching vibration of

Paper
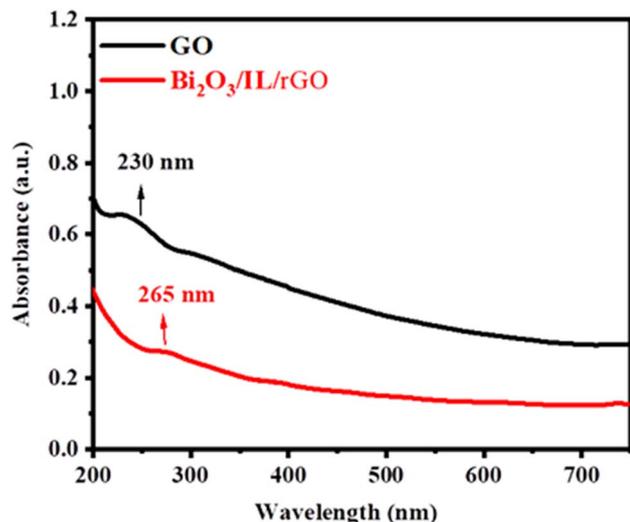
Fig. 2 UV-visible spectrum of GO and the $Bi_2O_3/IL/rGO$ nanocomposite.

COOH groups), 1393 cm^{-1} (OH bending vibration), and 1052 cm^{-1} (C–O stretching vibration), all clearly confirm that the GO was successfully synthesized.[20] Fig. 3(b) shows the FTIR spectrum of $Bi_2O_3/IL/rGO$. The first peak at 844 cm^{-1} is the stretching vibration of Bi–O.[21] The peak at 1074 cm^{-1} corresponds to C–N stretching.[22] The peaks at 1394 cm^{-1} and 1585 cm^{-1} correspond to the C–H bending and C=C from the reduced GO. The final peak at 1660 cm^{-1} is related to the C=C from incorporated the IL.[23]

3.3 XRD analysis of GO and the $Bi_2O_3/IL/rGO$ nanocomposite

X-ray diffraction spectroscopy (XRD) analysis was used to determine the crystal structures of GO and $Bi_2O_3/IL/rGO$ as shown in Fig. 4. A notable diffraction peak at a 2-theta angle of 10.60, which corresponds to the (001) plane of GO, is visible in
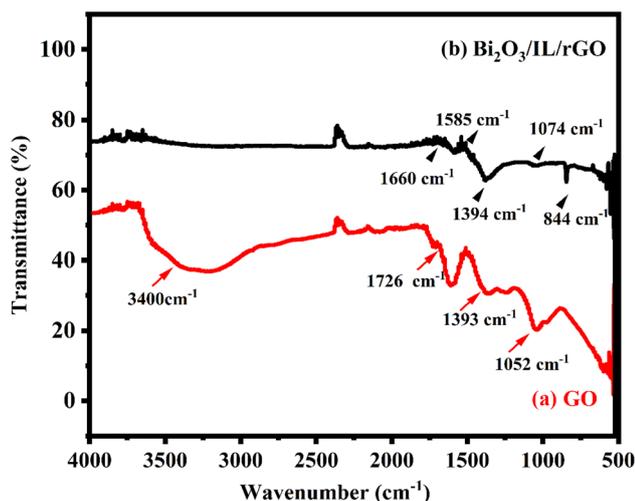
the XRD pattern of GO.[24] This peak confirms the existence of a functional group containing oxygen in the graphite oxide interlayer during the chemical synthesis of GO. Conversely, the 001 plane peak seen in GO is noticeably absent from the XRD pattern for the $Bi_2O_3/IL/rGO$ composite (black line). Instead, the 002 plane is represented by a new peak at 26.4, which shows that oxygen functional groups disappeared during the synthesis of the GO nanocomposite.[25] This result shows that GO was completely and successfully reduced to rGO within the composite. Additionally, the XRD pattern of Bi_2O_3 (shown in Fig. 4 as black plane numbers) shows intense and clear diffraction peaks at certain angles, which is strong evidence of the successful integration of Bi_2O_3 into the rGO structure. In contrast, the XRD pattern of the $Bi_2O_3/IL/rGO$ composite reveals distinct sharp peaks for the planes (020), (200), (021), (012) and (103) with other supported peaks that correspond to the lattice planes (102), (120), (121), (122), and (321). This comparison highlights the structural differences between GO and the $Bi_2O_3/IL/rGO$ composite, indicating the successful incorporation of bismuth oxide into the reduced graphene oxide matrix. The calculated crystalline size of prepared composite is 91.3 nm, which is equivalent to $Bi_2O_3/IL/rGO$ with a cubic structure. The particle size was determined using Debye–Scherer formula:

$$D = \frac{K\lambda}{\beta \cos \theta} \tag{1}$$

where the Bragg angle is denoted by θ, the corrected full width at half maximum by β, and the wavelength of the X-ray radiation by λ (Å). K is a constant that is commonly considered to be equal to one. The crystalline nature of the nanoparticles is revealed by the X-ray diffraction pattern. The diffraction peaks match those in the database (JCPDS card no. 6-294), confirming that the functionalised Bi_2O_3 nanocomposite was successfully synthesized.

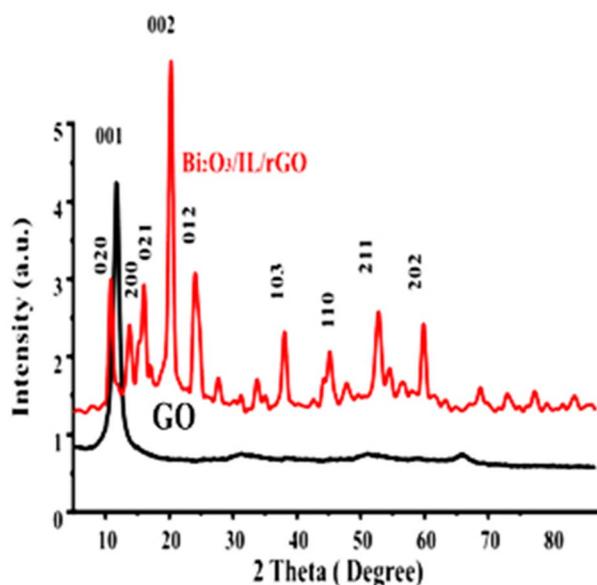Fig. 3 (a) FTIR spectrum of GO and (b) FTIR spectrum of $Bi_2O_3/IL/rGO$.

Fig. 4 X-ray diffraction (XRD) patterns of graphene oxide (GO) and the $Bi_2O_3/(IL/rGO)$ nanocomposite.
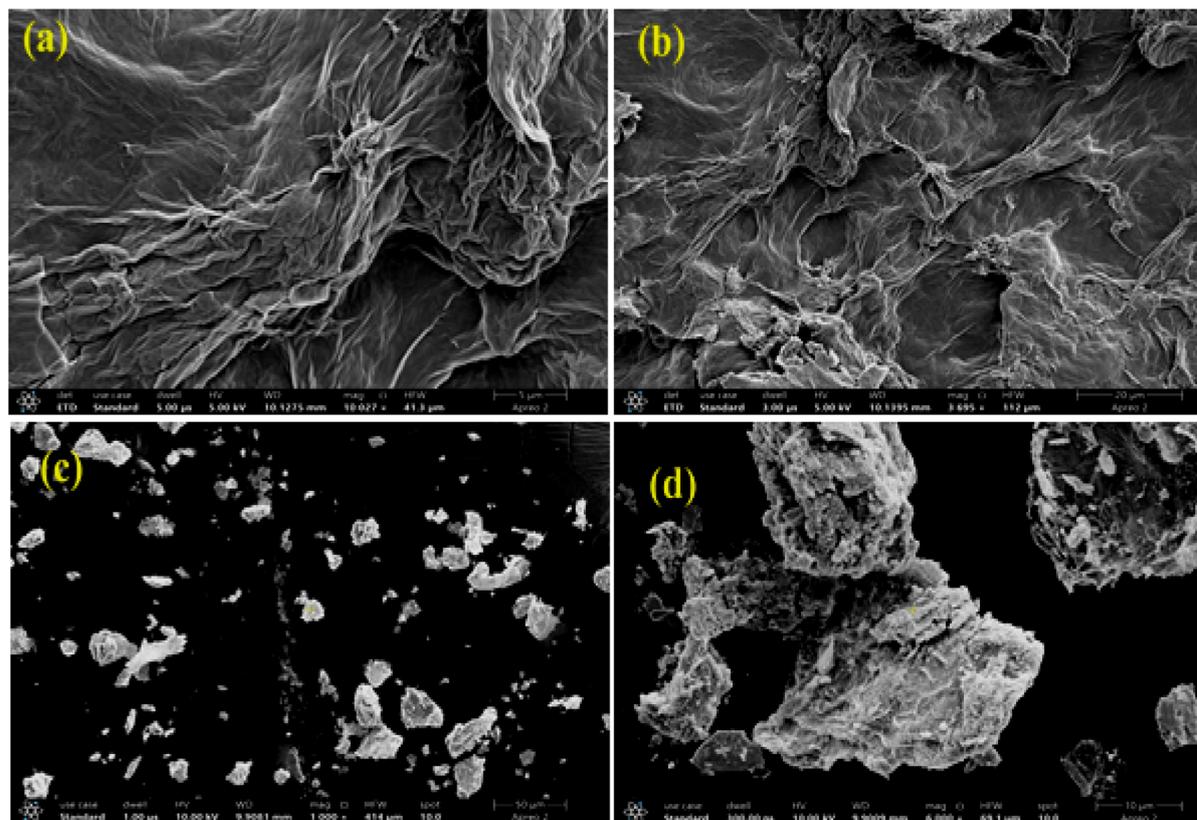
Fig. 5 (a) and (b) Scanning electron microscopy (SEM) images of graphene oxide (GO) and (c) and (d) SEM images of the Bi_2O_3/IL/rGO nanocomposite.

3.4 SEM analysis of GO and rGO

The 3D structure and morphology of the prepared composite material and graphene oxide (GO) were analyzed in detail using scanning electron microscopy (SEM). As illustrated in Fig. 5(a) and (b), the SEM image shows that GO has a distinctive sheet-like structure. There was a noticeable exfoliation and expansion of the GO sheets after adding Bi_2O_3/IL to the GO matrix. The SEM image in Fig. 5(c) and (d) illustrates that this change led to an increase in porosity and surface area. These modifications demonstrate the influence of composite fabrication on the of graphene oxide.

3.5 Elemental analysis of the Bi_2O_3/IL/rGO composite *via* energy dispersive spectroscopy (EDS)

Energy-dispersive X-ray spectroscopy (EDS) is an important method for determining the presence of specific elements within a sample. In this study, EDS analysis was conducted to determine the elemental composition of the Bi_2O_3/IL/rGO nanocomposite. The EDS spectrum shown in Fig. 6 indicates the presence of the basic elements, including carbon (C), oxygen (O), and bismuth (Bi). The analysis of the ratios of the main elements was predictable at 60.3% O, 36.1% C, and 3.6% Bi; these align well with the anticipated atomic ratios. Furthermore, the spectrum confirmed the presence of other elements connected with the ionic liquid used in the synthesis process.

The ionic liquid contributes carbon (C), fluorine (F), phosphorus (P) and oxygen (O) to the composite.

3.6 Electrochemical characterization of bare and modified electrodes

In electrochemical sensing, electrode characterization is important, as it relates to the catalytic activity, charge transfer kinetics and detection capabilities of the electrode. An important electrochemical method used in this analysis for initial electrode characterization was cyclic voltammetry (CV). Using a scan rate of 90 mV s^{-1}, bare and modified Bi_2O_3/IL/rGO/GCE
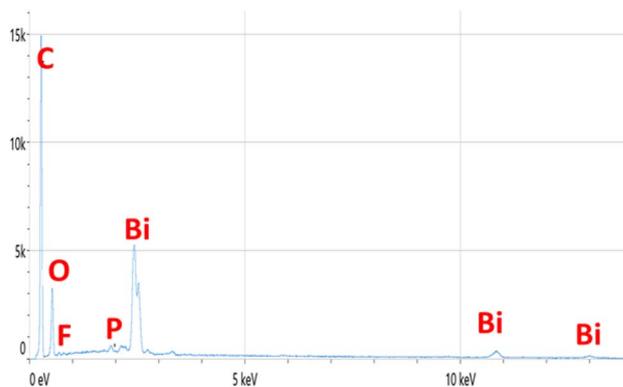

Fig. 6 Energy-dispersive X-ray (EDX) spectrum of the Bi_2O_3/IL/rGO nanocomposite.
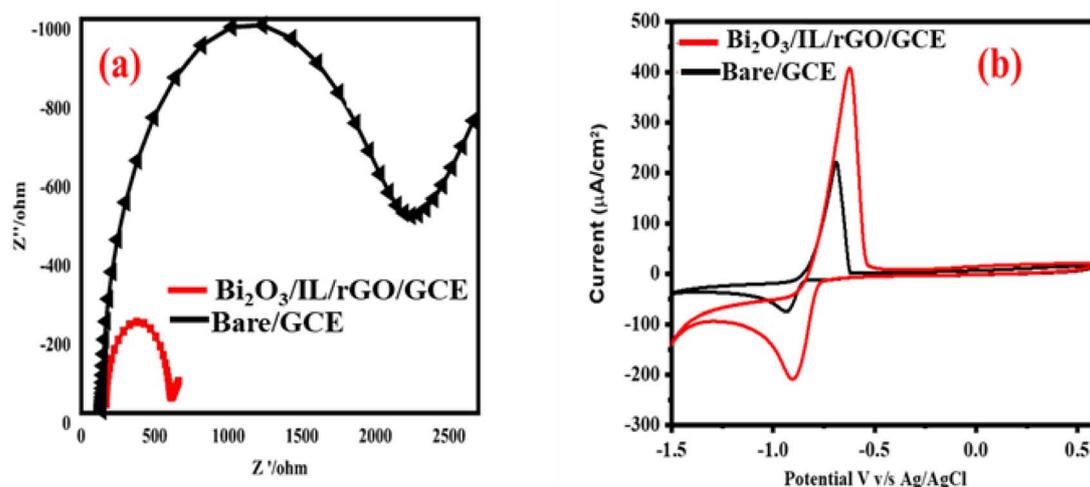
Fig. 7 (a) and (b) EIS and CV responses of bare GCE and $Bi_2O_3/IL/rGO/GCE$ in 0.5 mM $(K_4Fe(CN)_6)$ and 0.1 M KCl.

electrodes were examined in a solution of 0.5 mM $K_4[Fe(CN)_6]\cdot 3H_2O$ and 0.1 M potassium chloride. The experiments were repeated five times to ensure sensor reliability. The electrocatalytic characteristics and electron mobility of the $Bi_2O_3/IL/rGO$ composite were significantly enhanced by the incorporation of Bi_2O_3 nanoparticles into the GO structure. According to the CV curves, $Bi_2O_3/IL/rGO/GCE$ showed better results than the bare/GCE in terms of redox response, exhibiting distinct anodic and cathodic peaks as shown in Fig. 7(b). Furthermore, cross-

confirmation was conducted through electrochemical impedance spectroscopy (EIS) to assess the electrocatalytic characteristics and charge transfer kinetics. $Bi_2O_3/IL/rGO/GCE$ showed enhanced charge transfer kinetics, as seen in the Nyquist plot in Fig. 7(a). $Bi_2O_3/IL/rGO/GCE$ showed a much lower resistance (428.5 Ω) in the test solution than the bare GCE (1870 Ω). The high current responsiveness, decreased charge transfer resistance, and enhanced active surface area shown in the Nyquist plots contribute to the exceptional performance of $Bi_2O_3/IL/$

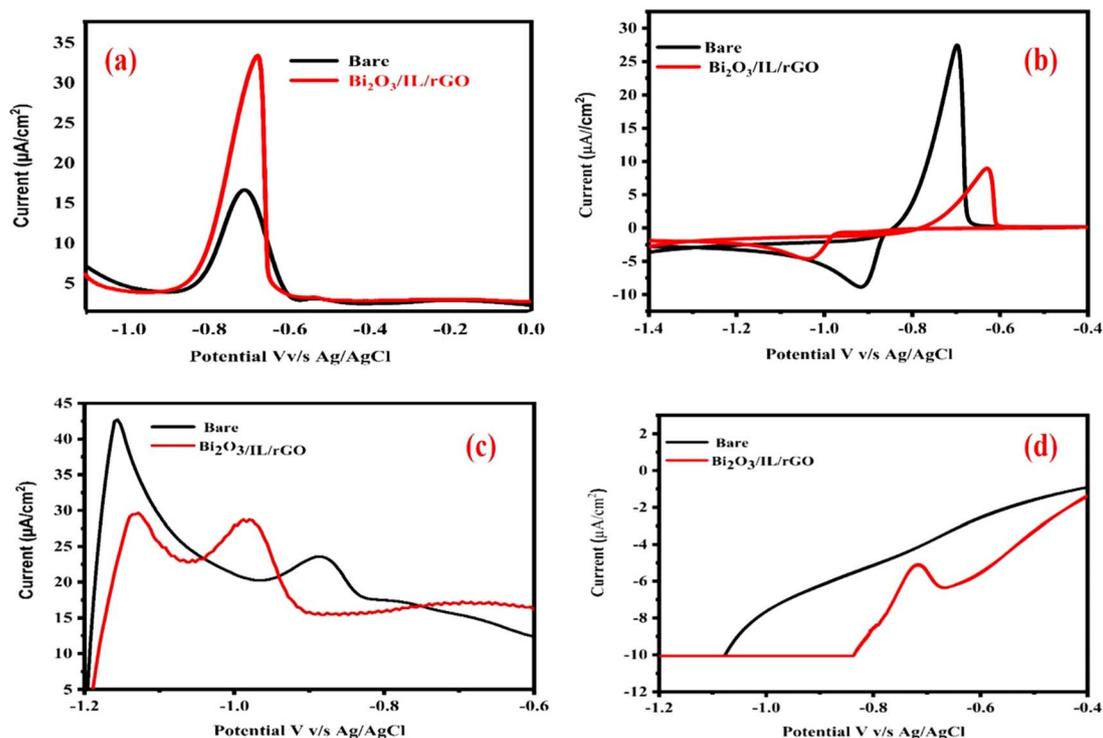**Fig. 8** Electrochemical responses of Pb^{2+} at a concentration of 20 μM evaluated using various voltammetric techniques: (a) differential pulse voltammetry (DPV), (b) square wave voltammetry (SWV), (c) linear sweep voltammetry (LSV), and (d) cyclic voltammetry (CV).

rGO/GCE, which makes it a viable option for the identification of Pb^{2+} in electrochemical sensing applications.

3.7 Different patterns of response for the bare and modified electrodes

The electrochemical responses to 20 µM Pb^{2+} in a 0.1 M phosphate electrolyte were examined at both the bare/GCE and Bi_2O_3/IL/rGO/GCE electrodes using several voltammetric techniques, including square wave voltammetry (SWV), linear sweep voltammetry (LSV), cyclic voltammetry (CV), and differential pulse voltammetry (DPV). Each technique was optimized using specific experimental settings. For CV, the potential window was −1.5 to 0.5 V and for DPV, the potential window was set from −1.0 to 0.0 V, with DPV utilizing an amplitude of 0.0 V, a pulse width of 0.05 s, a sample width of 0.0167 s, a pulse period of 0.2 s, a sample interval of 0.0001 V, and a quiet time of 0.3 s. The square wave voltammetry (SWV) method used an amplitude of 0.025 V, a frequency of 15 Hz, and a quiet time of 2 s, while LSV was performed with a scan rate of 0.1 V s^{-1}, a sample interval of 0.0001 V, and a quiet time of 3 s. Among these techniques, the DPV method yielded significantly higher peak currents compared to the other voltammetric methods. The results of all modes for Pb^{2+} are given in Fig. 8(a)–(d). The enhanced current response and sensitivity observed with DPV underscore its superior electrochemical performance for detecting Pb^{2+}. As demonstrated in Fig. 8(a), DPV proved to be the most effective and reliable method for accurate and efficient Pb^{2+} analysis across various samples.

3.8 Response to lead (Pb^{2+}) on bare and Bi_2O_3/IL/rGO/GCE

The determination of Pb^{2+} was performed using the differential pulse voltammetric (DPV) mode of electrochemical setup. To measure the effectiveness of method, we tested two electrodes, the bare/GCE and the Bi_2O_3/IL/rGO/GCE, quantifying their maximum responses to Pb^{2+}. This evaluation was conducted at a scan rate of 90 mV s^{-1} within a potential range of (−1.0 to 0.0 V), as displayed in Fig. 9. The results indicated an increase in the peak current for Bi_2O_3/IL/rGO/GCE, highlighting its enhanced electrochemical performance. This improvement can be attributed to the synergistic properties of reduced graphene oxide (rGO) combined with the unique electron transfer properties of bismuth oxide (Bi_2O_3). In comparison, the bare GCE demonstrated considerably lower peak currents, further emphasizing the greater sensitivity of the modified electrode for Pb^{2+} detection. Thus, Bi_2O_3/IL/rGO/GCE showed a more favorable response in Pb^{2+} analysis, showing its potential for real environmental monitoring.

3.9 Effect of supporting electrolytes

In electrochemical measurements, the supporting electrolytes create a conductive path for the analyte and sensing probes, facilitating effective electrochemical reactions. In this study, many supporting electrolytes were evaluated, including Britton–Robinson buffer (BRB) (pH 4, acidic), acetate (pH 9, basic), PBS (pH 6, slightly acidic), and borate (pH 8, slightly basic). The electrolytic detection of Pb^{2+} was examined at a scan rate of
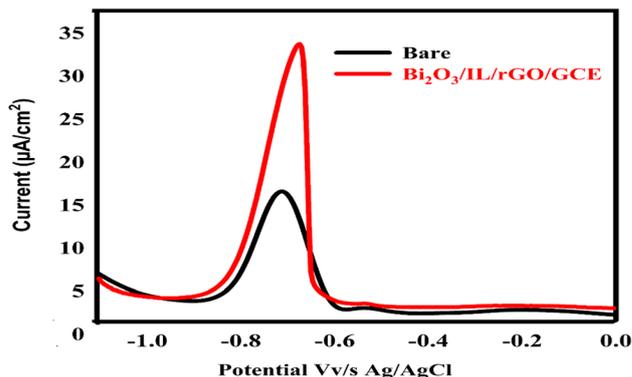
Fig. 9 DPV response of the bare/GCE and Bi_2O_3/IL/rGO/GCE in the presence of 20 µM lead Pb^{2+}.
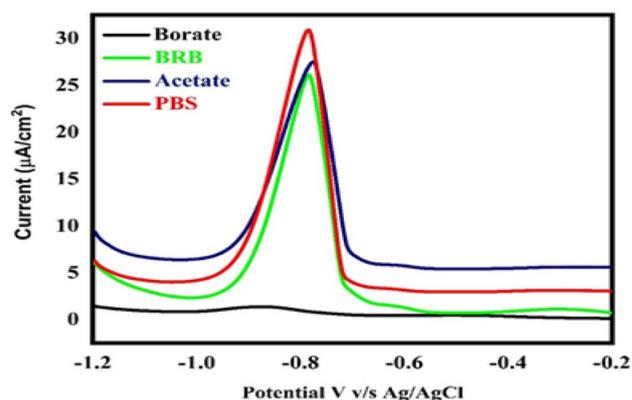
Fig. 10 Ipa responses to 20 µM Pb^{2+} in different electrolytic systems ranging from acidic to basic pH.

90 mV s^{-1} with a concentration of 20 µM Pb^{2+}. This efficient analysis enhanced our understanding of how various electrolytes influence lead detection. The results indicated that PBS buffer provided better peak shape, resolution, and sensitivity
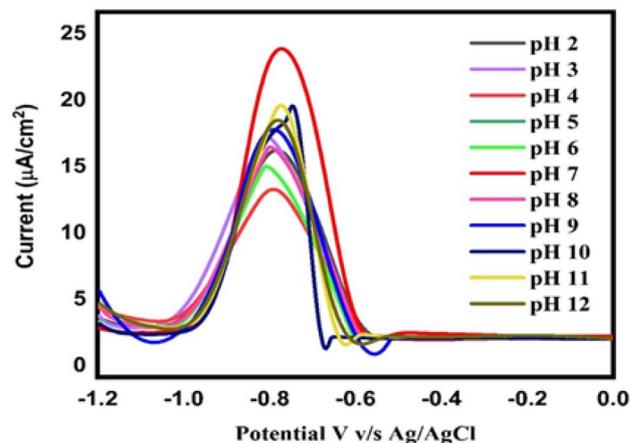
Fig. 11 DPV responses of Bi_2O_3/IL/rGO/GC to 20 µM Pb^{2+} in 0.1 M phosphate at different pH values ranging from 2.0–12.0.

Fig. 12 (a) Scan rate impact on the redox reaction of Pb^{2+}. (b) Anodic peak current response plot with $R^2 = 0.98$ and $R^2 = 0.97$ for the redox peak current response plot with changing the scan rate from 10 to 90 mV s^{-1}.

compared to Britton–Robinson, acetate, and borate buffer, as shown in Fig. 10. Consequently, PBS was chosen as the supporting electrolyte for further experiments.
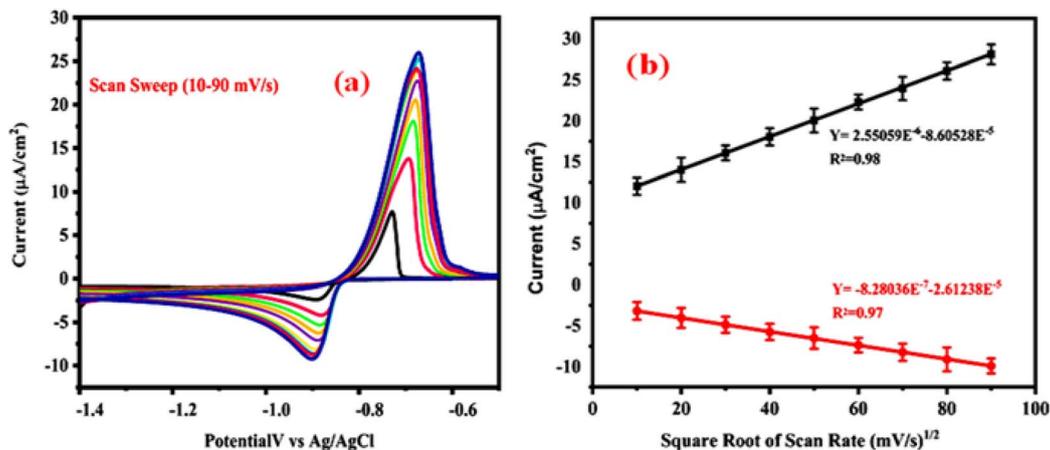
3.10 Effect of pH

Many electrochemical sensors depend on the pH to function properly. The stability and reactivity of the electrode material are two significant factors related to pH. At specific pH levels, certain electrode materials can develop corrosion or undergo chemical reactions that change the sensor function over time. The current and peak potential response to the targeted analyte are additionally affected by the pH. Therefore, a range of PBS electrolyte pH values, from an acidic pH of 2 to a basic pH of 12, were used in order to assess the impact of pH on the Ipa response of Pb^{2+}, as presented in Fig. 11. The DPV response was measured in numerous solutions of the supporting electrolyte with different pH values, and revealed a clear dependence of the current on the pH of the electrolyte. An increased Ipa response to the analyte was seen at PBS pH 7 compared to the other electrolytes. Fig. 11 shows the distinct current responses to Pb^{2+}

at different pH values. The PBS electrolyte with a pH of 7 was chosen for additional optimisations after the pH-based current response was assessed. This pH study enabled the highest current response and efficient electrochemical detection of Pb^{2+}.

3.11 Effect of scan rate

The adsorption or diffusion control of the Bi_2O_3/IL/rGO/GCE process was effectively investigated through scan rate measurements. Scan rate serves as a key parameter to determine whether ions are moving freely or adhering to the electrode surface. An increase in scan rate from lower to higher values typically results in an enhanced response to the analyte, provided the that the electrode is uniformly deposited. Cyclic voltammetry was used to examine the diffusion-controlled process and redox response to lead ions at the modified electrode surface.

To assess the impact of scan rate on the Ipa response of Pb^{2+} at Bi_2O_3/IL rGO/GCE, the scan rate was increased from 10 to 90 mV s^{-1}, as shown in Fig. 12(a). The Bi_2O_3/IL rGO/GCE

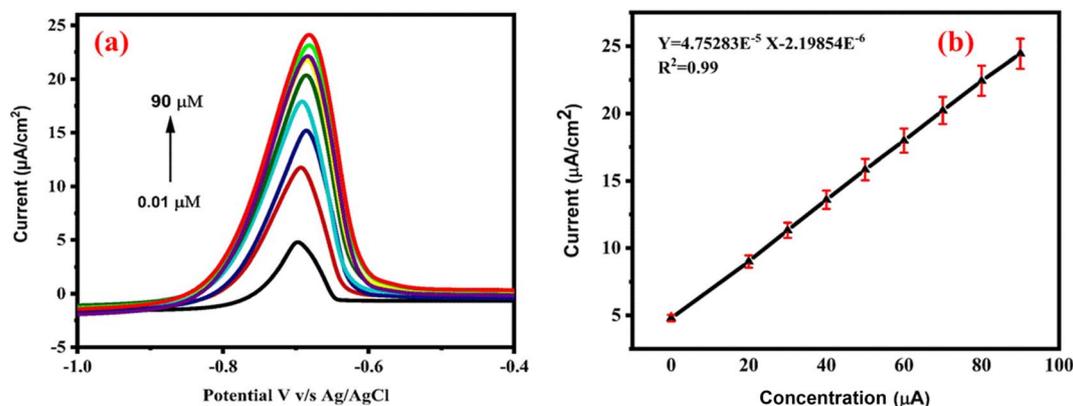**Fig. 13** (a) DPV-based calibration current response to Pb^{2+} for concentrations ranging from 0.01 to 90 μM; (b) linearity of calibration, with $R^2 = 0.99$.

Table 1 Analytical performance of the developed $Bi_2O_3/IL/rGO/GCE$ sensor for Pb^{2+} as compared to previous studies

Sensor	Technique	Linear range (μM)	LOD (μM)	Reference
PtNPs/rGO/GCE	DPV	0.05–10	0.015	26
Au–Ag NTs/NG	DPV	0.1–420	0.015	27
Meso-Co_3O_4/RGO/GCE	DPV	0.1–300	0.03	28
Fe_3O_4	DPV	0.04–20.0	0.0595	29
Pd1.5/PAC-900	DPV	0.5–8.9	0.05	30
$MnFe_2O_4$@Cys	DPV	0.1–1.0	0.0843	31
BD-NCD	DPV	1–22.5	1.339	32
Sb_2O_3/MWCNTs	SWASV	0.024–0.169	0.013	33
MWCNT/SPCE	SWASV	81.7–559.2	24.4	34
NF/G/PANI	SWASV	5.55–1665.5	0.55	35
PA/PPy/GO	SWASV	27.7–832.8	2.28	36
Al_4SiC_4/RGO/GCE	SWASV	277.5–14964.4	7.22	37
BI/MWNT-IL/SPCE	SWASV	5.55–333.3	0.666	38
Bi/LGR/GCE	SWASV	27.7–666.6	2.28	39
ZnO@G/GCE	SWASV	55.5–1110	4.44	40
Bi_2Te_3/GO/GCE	SWASV	2.77–111.1	1.11	41
IL-rGO/AuNDs/Nafion	SWV	300 000–100	0.035	42
Thionine/graphene	DPV	$1.6 \times 10^{-7} - 1.6 \times 10^{-4}$	3.2×10^{-14}	43
Thionine/porousAu-PdNPsa	DPV	$10–12 \times 10^{-7}$	3.4×10^{-13}	44
Cu_2O–Au/NG/GCE	DPSV	0.05–100	0.03	45
Cu–Cs/MWCNT/GCE	DPSV	0.05–100	0.01	46
$Bi_2O_3/IL/rGO/GCE$	**DPV**	**0.01–90**	**0.001**	**This work**

exhibited an excellent redox response to lead ions at increased scan sweep rates. The increase in scan rate correlated with a linear increase in the Ipa response to Pb^{2+} at Bi_2O_3/IL rGO/GCE, indicating its favorable electrocatalytic properties and diffusion-controlled behavior. The linearity of the Pb^{2+} redox response was confirmed using a regression equation, which yielded R^2 values of 0.98 for oxidation and 0.97 for the reduction peak current response, as depicted in Fig. 12(b).

3.12 Calibration study

Calibration plays a crucial role in ensuring the accuracy and reliability of electrochemical sensors by comparing the output signal of the sensor to a known standard or reference material.

This process is essential, as environmental factors such as temperature, humidity, and interference from other chemicals can affect the response of the sensor. Without proper calibration, the sensor may yield inaccurate or inconsistent measurements, which could lead to erroneous conclusions or decisions. In current study, the concentration range for the calibration measurement was set from 0.01 to 90 μM. The $Bi_2O_3/IL/rGO/GCE$ exhibited an excellent linear response to Pb^{2+}, as shown in Fig. 13(a). The linearity of the current responses to Pb^{2+} was determined using a regression equation, resulting in an R^2 value of 0.99, as shown in Fig. 13(b). Furthermore, using the calibration data, the limit of detection (LOD) and limit of quantification (LOQ) were calculated using the formulas 3SD of blank/slope and
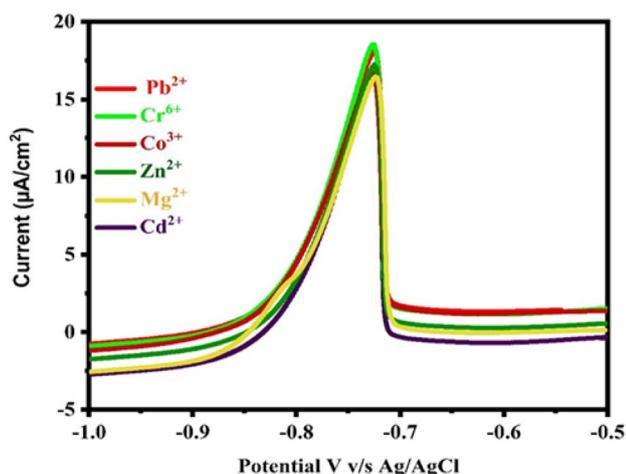

Fig. 14 Effect of interfering substances on Ipa response to 20 μM Pb^{2+} in 0.1 M PBS (pH 7.0).
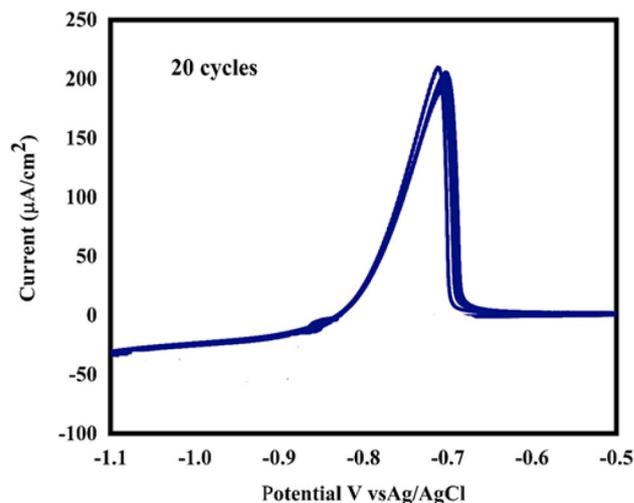

Fig. 15 Stability of $Bi_2O_3/IL/rGO/GCE$ in the presence of 20 μM Pb^{2+}.

10SD of blank/slope. The slope was derived from the calibration curve, and the standard deviation (SD) of the blank was obtained from the current values ($n = 5$) of the Bi_2O_3/IL/rGO/GCE in PBS electrolyte at pH 7. The calculated LOD and LOQ for the developed method were 0.001 μM and 0.03 μM, respectively. Furthermore, to assess the sensitivity, effectiveness, and reliability of the Bi_2O_3/IL/rGO/GCE, the proposed sensor was compared with reported sensors used for detecting Pb^{2+}. The comparison presented in Table 1 shows that the current method is effective and reliable compared to the reported sensors. Moreover, the fabricated sensor is capable of detecting Pb^{2+} at lower concentration levels compared to the reported sensors. This could be considered a limitation of the current method compared to other reported sensors. The sensor displays strong responsiveness to lead ions due to its tailored nanocomposite structure. It ensures precise measurements even at very low concentrations, which is vital for environmental monitoring. Fast electron movement and stable signal output are achieved through the inclusion of the ionic liquid and rGO. The eco-conscious design avoids toxic materials, offering a safer alternative for heavy metal sensing. The sensor remains effective across various real-world water samples, showing its practical reliability.

3.13 Effect of interferents

The reliability and effectiveness of the developed Bi_2O_3/IL/rGO/GCE sensor was tested with various interferents. Each sample run was repeated five times ($n = 5$) to ensure the accuracy of the experiment. The selectivity of the developed sensor was evaluated by testing it on a variety of metal ions, including Zn^{2+}, Co^{2+}, Cd^{2+}, Mg^{2+} and Cr^{6+}. The results showed that these ions had no apparent effect on the lead detection. Based on the results in Fig. 14, it can be concluded that the concentrations of the potential interferents had no effect on the highest peak current. The relative standard deviation (RSD) value obtained for

Table 2 Pb^{2+} levels in soil and wastewater samples measured using a Bi_2O_3/IL/rGO/GCE sensor

Sample	Spiked (μM)	Detected (μM)	RSD (%)	Recovery (%)
Industrial area soil	0	1.78	0	0
	5	6.58	1.91	96
	10	16.08	2.27	95
	15	30.58	1.28	96.6
Pharmaceutical industrial wastewater	0	1.86	0	0
	5	6.76	3.09	98
	10	16.66	1.10	96
	15	31.26	3.84	97.3
Vegetable field water	0	1.60	0	0
	5	6.65	4.9	101
	10	16.6	3.18	99.5
	15	31.6	3.83	100
Textile 1	0	1.68	0	0
	5	6.99	1.44	97.8
	10	16.7	2.57	95.5
	15	31.02	1.82	96.7
Automobile	0	1.49	0	0
	5	6.79	1.10	102
	10	16.4	1.25	97.6
	15	29.99	1.95	96.6
Detergent/soap industry	0	1.76	0	0
	5	6.56	1.96	96.5
	10	16.3	1.06	98
	15	31.1	3.06	98
Textile 2	0	1.97	0	0
	5	6.96	2.27	95
	10	16.29	1.14	97.9
	15	31.28	2.42	95.8
Tannery	0	1.66	0	0
	5	6.81	2.15	96
	10	15.6	3.96	98
	15	31.9	2.14	96.2
Textile 3	0	1.73	0	0
	5	6.59	1.63	97.1
	10	16.2	1.14	98
	15	32	2.17	96.7
Pharma	0	2.96	0	0
	5	6.81	1.50	102
	10	16.9	3.13	99.3
	15	31.8	1.78	96.8

interference was 2.85%, which is below 5%. These results indicate the proposed sensor is not significantly affected by interfering species, indicating the selective behavior of the $Bi_2O_3/IL/rGO/GCE$ for Pb^{2+} detection.

3.14 Stability of $Bi_2O_3/IL/rGO/GCE$

The stability of the $Bi_2O_3/IL/rGO/GCE$ was assessed through 20 repeated experiments using 20 μM Pb^{2+} solutions in 0.1 M phosphate buffer at pH 7.0, as shown in Fig. 15. The currents measured for the $Bi_2O_3/IL/rGO/GCE$ *via* the DPV method demonstrated good stability, with a relative standard deviation (RSD) of 2.96% for Pb^{2+}. These results indicated that the $Bi_2O_3/IL/rGO/GCE$ exhibits excellent stability.

3.15 Real sample analysis

The $Bi_2O_3/IL/rGO$ electrode was tested for the detection of Pb^{2+} in a variety of water and soil samples to evaluate its effectiveness. Soil and wastewater samples were collected from Tandoallahyar and Karachi, Sindh, Pakistan. To prepare the samples for analysis, they were first filtered through Whatman filter paper. Once adequately mixed, 9 mL of the supporting electrolyte was added to 1 mL of the wastewater sample in a 10 mL electrochemical cell. The soil samples were prepared through a digestion process, enabling a thorough assessment of the lead content in both the soil and wastewater samples. The suggested method has been validated. The percentage recovery varied between 95 and 105%, according to the data. The relative standard deviation of each run was determined by calculating the mean and standard deviation of three separate measurements. The RSD values were found to be between 1.02 to 3.96%, which validated the accuracy and precision of the modified electrode (Table 2).

4.   Conclusion

In this study, $Bi_2O_3/IL/rGO$ was effectively synthesized and characterized using advanced analytical devices. Subsequently, a glassy carbon electrode was modified with $Bi_2O_3/IL/rGO$ to develop an electrochemical sensor for the effective detection of Pb^{2+}. The sensor demonstrated excellent performance, attaining a low limit of detection (LOD) of 0.001 μM and limit of quantification (LOQ) of 0.003 μM, through a broad linear dynamic range from 0.01 to 90 μM. Moreover, it exhibited excellent stability, sensitivity, and selectivity under optimal conditions, allowing for dependable and uniform detection in complex matrices. The accuracy and validity of the sensor were evaluated using real samples, such as soil and wastewater, which confirmed its reliability and effectiveness in practical applications. Additionally, the sensor maintained its performance over extended periods, demonstrating impressive long-term stability. Overall, the research illustrates applications while introducing an exceptional and viable method for the efficient detection of lead. Our results highlight the importance of emerging advanced materials for electrochemical sensing, paving the way for future improvements in environmental analytics and safety. Despite all the advantages of the prepared

material, it may have certain limitations, such as the fabrication process of the nanocomposite involving various steps, which makes it slightly complex and slow. Furthermore, the long-term stability and repeatability could affect the performance of the sensor.

However, the current study offers important cost savings in the fabrication and maintenance of the sensor, making it a reasonable alternative to current technologies. The simple design of the sensor confirms its straightforward operation, and minimal technical expertise. Its greater sensitivity allows for accurate measurements at lower concentrations and successful detection capabilities. These advantages make the sensor a valuable technique for significant environmental monitoring and early hazard identification.

Data availability

The data will be available.

Author contributions

Sanoober Bhagat: conceptualization, methodology, formal analysis, and original draft preparation. Sana-ul-Nisa: formatting, investigation, and data compilation. Jamil A. Buledi: editing and review of the manuscript. Amber R. Solangi: supervision, resources, and project administration, visualization, validation, and S. Tufail H. Sherazi: critical review, and final approval of the manuscript. Each author contributed significantly to the research, ensuring the accuracy and integrity of the work presented.

Conflicts of interest

The authors declare no conflict of interest associated with this work.

Acknowledgements

References

1 V. J. W. Saxena, *Water, Air, Soil Pollut.*, 2025, **236**, 1–40.
2 S. Fang, C. Hua, J. Yang, F. Liu, L. Wang, D. Wu and L. Ren, *J. Hazard. Mater.*, 2025, **485**, 136812.
3 Y. Nthwane, B. Fouda-Mbanga, M. Thwala and K. J. E. T. Pillay, *Environ. Technol.*, 2025, **46**, 414–430.
4 S. Zafar, S. Fatima, F. Asad, M. M. Nazir, S. Batool and A. J. W. Ashraf, *Water, Air, Soil Pollut.*, 2025, **236**, 8.
5 Y. Ji, J. Xu, S. Wang, B. Xue, C. Li, X. Zhang, X. Yang, Z. Qiu, J. Wang, X. J. S. Xiao, C. Zhao and Z. Shen, *Sens. Actuators, B*, 2025, **430**, 137254.
6 R. Singh, R. Gupta, D. Bansal, R. Bhateria and M. Sharma, *ACS Omega*, 2024, **9**, 7336–7356.

7 D. Yang, X. Wang and H. Xu, *Catalysts*, 2024, **14**, 451.

8 C. Wang, Q. Niu, D. Liu, X. Dong and T. You, *Talanta*, 2023, **258**, 124281.

9 E. C. Okpara, R. D. Crapnell, E. Bernalte, O. B. Wojuola and C. E. Banks, *Electroanalysis*, 2025, **37**, 12019.

10 X. Hao, W. Song, Y. Wang, J. Qin and Z. J. Jiang, *Small*, 2025, **21**, 2408624.

11 M. Wu, B. Xu, Y. Zhang, S. Qi, W. Ni, J. Hu and J. Ma, *Chem. Eng. J.*, 2020, **381**, 122558.

12 S. Aldroubi, N. Brun, I. B. Malham and A. Mehdi, *Nanoscale*, 2021, **13**, 2750–2779.

13 P. Verma, R. Chowdhury and A. Chakrabarti, *J. Mater. Sci.*, 2021, **56**, 19329–19358.

14 N. Munusamy, F. P. D. Disouza, S.-M. Chen, K. Krishnan, M. K. D. Jothinathan and B. Prakash, *J. Taiwan Inst. Chem. Eng.*, 2024, **165**, 105708.

15 M. Fathi, *J. Chem. Biol. Med. Sci.*, 2025, **1**, 167–173.

16 U. Choudhari, N. Ramgir, C. Vaghela, S. Jagtap and K. Muthe, *Microchem. J.*, 2024, **202**, 110763.

17 D. Das, U. K. Panigrahi, J. Giri, A. K. Panda, P. K. Satapathy and P. Mallick, *J. Photochem. Photobiol., A*, 2024, **457**, 115912.

18 N. S. Singh, A. K. Mia and P. Giri, *Nanoscale Adv.*, 2024, **6**, 2136–2148.

19 A. I. El-Batal, G. S. El-Sayyad, A. El-Ghamry, K. M. Agaypi, M. A. Elsayed and M. Gobara, *J. Photochem. Photobiol., B*, 2017, **173**, 120–139.

20 M. Ebrahimi Naghani, M. Neghabi, M. Zadsar and H. Abbastabar Ahangar, *Sci. Rep.*, 2023, **13**, 1496.

21 A. Doma, M. I. Abbas, B. K. Abd El Hady, E. A. Ghafeir and A. El-Khatib, *Ceram. Int.*, 2025.

22 X. Hu, J. Wang, J. Wang, Y. Deng, H. Zhang, T. Xu and W. Wang, *Appl. Catal., B*, 2022, **318**, 121879.

23 V. Brusko, A. Khannanov, A. Rakhmatullin and A. M. Dimiev, *Carbon*, 2024, **229**, 119507.

24 M. Akbarpour and F. G. Asl, *Ceram. Int.*, 2023, **49**, 13829–13835.

25 S. M. Mbam, R. M. Obodo, O. O. Apeh, A. C. Nwanya, A. Ekwealor, N. Nwulu and F. I. Ezema, *J. Mater. Sci.:Mater. Electron.*, 2023, **34**, 1405.

26 P. Pang, H. Li, Y. Liu, Y. Zhang, L. Feng, H. Wang, Z. Wu and W. Yang, *Anal. Methods*, 2015, **7**, 3581–3586.

27 B. Yang, D. Bin, K. Zhang, Y. Du and T. Majima, *J. Colloid Interface Sci.*, 2018, **512**, 446–454.

28 J. Zhang, S. Cui, Y. Ding, X. Yang, K. Guo and J. Zhao, *Ceram. Int.*, 2018, **44**, 7858–7866.

29 W.-J. Li, X.-Z. Yao, Z. Guo, J.-H. Liu and X. J. Huang, *J. Electroanal. Chem.*, 2015, **749**, 75–82.

30 P. Veerakumar, V. Veeramani, S.-M. Chen, R. Madhu and S. B. Liu, *ACS Appl. Mater. Interfaces*, 2016, **8**, 1319–1326.

31 S.-F. Zhou, J.-J. Wang, L. Gan, X.-J. Han, H.-L. Fan, L.-Y. Mei, J. Huang and Y. Q. Liu, *J. Alloys Compd.*, 2017, **721**, 492–500.

32 E. Nurhayati, Y. Juang, M. Rajkumar, C. Huang and C. C. Hu, *Sep. Purif. Technol.*, 2015, **156**, 1047–1056.

33 S. Yang, P. Liu, Y. Wang, Z. Guo, R. Tan and L. Qu, *RSC Adv.*, 2020, **10**, 18526–18532.

34 C. Pérez-Ràfols, N. Serrano, J. M. Díaz-Cruz, C. Ariño and M. Esteban, *Anal. Chim. Acta*, 2016, **916**, 17–23.

35 N. Ruecha, N. Rodthongkum, D. M. Cate, J. Volckens, O. Chailapakul and C. S. Henry, *Anal. Chim. Acta*, 2015, **874**, 40–48.

36 H. Dai, N. Wang, D. Wang, H. Ma and M. Lin, *Chem. Eng. J.*, 2016, **299**, 150–155.

37 Y. Wu, T. Yang, K.-C. Chou, J. Chen, L. Su and X. Hou, *Analyst*, 2017, **142**, 2741–2747.

38 H. Wang, G. Zhao, Z. Zhang, Y. Yi, Z. Wang and G. Liu, *Int. J. Electrochem. Sci.*, 2017, **12**, 4702–4713.

39 X. Lin, Z. Lu, Y. Zhang, B. Liu, G. Mo, J. Li and J. Ye, *Microchim. Acta*, 2018, **185**, 1–9.

40 J. Yukird, P. Kongsittikul, J. Qin, O. Chailapakul and N. Rodthongkum, *Synth. Met.*, 2018, **245**, 251–259.

41 F. Tseliou, A. Avgeropoulos, P. Falaras and M. I. Prodromidis, *Electrochim. Acta*, 2017, **231**, 230–237.

42 F. Li, D. Pan, M. Lin, H. Han, X. Hu and Q. Kang, *Electrochim. Acta*, 2015, **176**, 548–554.

43 F. Gao, C. Gao, S. He, Q. Wang and A. Wu, *Biosens. Bioelectron.*, 2016, **81**, 15–22.

44 Q. Zhou, Y. Lin, Y. Lin, Q. Wei, G. Chen and D. Tang, *Biosens. Bioelectron.*, 2016, **78**, 236–243.

45 S. Li, B. Yang, C. Wang, J. Wang, Y. Feng, B. Yan, Z. Xiong and Y. Du, *J. Electroanal. Chem.*, 2017, **786**, 20–27.

46 M. B. Gholivand, L. Mohammadi-Behzad and H. Hosseinkhani, *Anal. Biochem.*, 2016, **493**, 35–43.